Materialia 25 (2022) 101538

Contents lists available at ScienceDirect

Materialia

journal homepage: www.elsevier.com/locate/mtla

Computational analysis of heterogeneous nucleation and precipitation in AA6005 Al-alloy during continuous cooling DSC experiments

Bernhard Miesenberger[a,*], Ernst Kozeschnik[b], Benjamin Milkereit[c,d], Piotr Warczok[e], Erwin Povoden-Karadeniz[a,b]

[a] Christian Doppler Laboratory for Interfaces and Precipitation Engineering CDL-IPE, Institute of Materials Science and Technology, TU Wien, Getreidemarkt 9, 1060, Vienna, Austria
[b] Institute of Materials Science and Technology, TU Wien, Getreidemarkt 9, 1060, Vienna, Austria
[c] Chair of Materials Science, Faculty of Mechanical Engineering and Marine Technology, University of Rostock, Justus-von-Liebig-Weg 2, 18059, Rostock, Germany
[d] CALOR – Competence Centre Thermal analysis and Calorimetry Rostock, Department Life, Light & Matter, University of Rostock, Albert-Einstein-Str. 25, Rostock, Germany
[e] MatCalc Engineering GmbH, Gumpendorferstraße 21, 1060 Vienna, Austria

A B S T R A C T

A physically-based model for the computational evaluation of differential scanning calorimetry (DSC) curves during continuous cooling of Al alloys from solution annealing temperature is developed. The model is particularly suitable for predicting the nucleation and growth of quench induced precipitates at heterogeneous nucleation sites, such as grain boundaries, the stress field of dislocations or particles like primary phases or dispersoids. The thermokinetic model incorporates an extended formulation of the precipitate nucleation barrier and considers β-Mg_2Si and B'-$Al_4Mg_8Si_7$ phase precipitates. These are the dominating, experimentally observed quench induced phases in an aluminium AA6005 alloy within a wide range of cooling rates. The model is implemented in the thermokinetic software MatCalc, which simulates the precipitation processes and the evolution of excess specific heat capacities during the heat treatments. The Generalized Broken Bond model, incorporating the effects of interface curvature and diffuse interfaces, is used for interface energy prediction. Comparison of experiment and simulation demonstrates that the impact of heterogeneous nucleation sites must be adequately considered in the nucleation energy expression to obtain accurate predictions of the precipitate evolution, particularly for precipitation at low and very low undercooling as present during continuous cooling, particularly at slower cooling rates.

1. Introduction

Precipitation of Mg-Si phases during cooling after solution treatment or homogenization in Al-alloys affects the microstructural changes during subsequent artificial ageing or pre-heating of hot forming processes [1–6]. An in-depth understanding of the kinetics of precipitation will allow for predictions on these microstructural changes and thus assist the production of material with optimized properties. During cooling of solution-treated Mg- and Si-alloyed AA6xxx Al-alloys, thermodynamically stable β and metastable Al-containing Mg-Si B'-phases form. The cubic β-Mg_2Si phase occurs as incoherent precipitates with the stoichiometry β-Mg_2Si [7]. Dumolt et al. [8] detected the B'- $Al_4Mg_8Si_7$ phase as a lath-like precipitate growing along the <100> directions of the matrix. A thermodynamic description of these phases has been suggested by Povoden-Karadeniz et al. [9].

A well-established experimental method to investigate precipitation reactions is differential scanning calorimetry (DSC) [10–13]. Most of this research has focused on continuous heating DSC. A comparison of experimental continuous heating DSC results with computer simulation of heat flow and phase precipitation has been carried out by, e.g., Lang et al. [14,15] or Falahati et al. [16]. Milkereit and coworkers have extensively investigated precipitation reactions during cooling from elevated temperatures by DSC, including a range of Al-alloys within the AA6xxx series [17–21]. These authors have analyzed the relation between different cooling rates and the evolution of the equilibrium β-Mg_2Si and metastable $Al_4Mg_8Si_7$ B'-phase at heterogeneous nucleation sites, such as grain boundaries or particles like primary phases for β-Mg_2Si phase precipitates [17,20,22] and dispersoids for B'-$Al_4Mg_8Si_7$ phase precipitates [17,19,20]. In 6xxx alloys, primary phases are AlFeMnSi-phases at grain boundaries, which form during casting. Dispersoids nucleate in the matrix at β'-phase during first re-heating after casting at about 350°C [23] and have a similar composition and structure as primary phases.

An appropriate understanding of the energetics of heterogeneous precipitation is required to conduct predictive simulations of precipitation during continuous cooling. In the current modeling approach, heterogeneous nucleation site energies are considered in evaluating the nucleation barrier for the precipitation reactions, emphasizing the case of low and very low undercooling. In the model formulation, the nucleation event will compensate some part of the heterogeneous nucle-

* Corresponding author at: Institute of Materials Science and Tecnology, Technical University of Vienna: Technische Universitat Wien, Getreidemarkt 9, 1060, Vienna, Austria.
E-mail address: bernhard.miesenberger@gmail.com (B. Miesenberger).

https://doi.org/10.1016/j.mtla.2022.101538
Received 31 January 2022; Accepted 6 August 2022
Available online 10 August 2022

ation site energy and thus, potentially facilitate the nucleation process. Only with these considerations, a sound prediction of precipitate nucleation during slow cooling below solution temperature is successfully achieved.

2. Modeling

In the following, the advanced model for precipitate nucleation is outlined as developed in the present work. Supchapters 2.1 to 2.3 are written in a universal way and are not restricted to typical nucleation mechanisms in aluminium 6xxx alloys.

Emphasis is placed on continuous cooling conditions. The main challenge of the simulation is the correct representation of the nucleation conditions at heterogeneous nucleation sites, such as grain boundaries (faces, edges, and corners), dislocations and primary or dispersoid particles, with the boundary condition that nucleation occurs at low and very low undercooling (supersaturation). These conditions are typical for continuous cooling DSC experiments at low cooling rates where the phase boundaries of precipitates are approached from the high-temperature region. It is also demonstrated that the impact of heterogeneous nucleation sites becomes increasingly prominent with decreasing cooling rate.

2.1. Classical precipitate nucleation

In the framework of classical nucleation theory (CNT) [24], the transient nucleation rate, J, is the governing model parameter for precipitation kinetics simulations during heat treatment of an alloy. It is commonly written as [25]

$$J = N_0 Z \beta^* exp\left(\frac{-G^*}{k_B T}\right) exp\left(\frac{-\tau}{t}\right) \tag{1}$$

where N_0 is the number of potential nucleation sites, Z is the Zeldovich factor, β^* is the atomic attachment rate, G^* is the critical nucleation energy, k_B is the Boltzmann constant, τ is the incubation time, t is time, and T is temperature. This critical nucleation energy, G^*, strongly determines J. It is commonly derived from the extremum value of the nucleation energy

$$\Delta G_{nucl}^{CNT} = \frac{4}{3}\pi\rho^3 \Delta G_{vol} + 4\pi\rho^2 \Delta G_{intf} \tag{2}$$

where ΔG_{nucl}^{CNT} is the CNT free energy of nucleus formation. In conventional CNT, ΔG_{nucl} depends only on the radius of the nucleus, ρ, whereas the volume free energy change, ΔG_{vol}, and the specific interface energy, ΔG_{intf}, are constant and independent of the nucleus size. Under these conditions, the critical nucleation barrier is straightforwardly obtained with

$$G_{CNT}^* = \frac{16}{3}\pi \frac{\left(\Delta G_{intf}\right)^3}{\left(\Delta G_{vol}\right)^2} \tag{3}$$

which can be inserted directly into Eq. (1) to obtain the nucleation rate of the precipitation process.

2.2. Temperature- and size-dependent interface energy

In CNT and its application to precipitation modeling, the interface free energy, ΔG_{intf}, is often a (constant) fitting parameter to match the computed evolution of precipitation parameters to experimental data, such as phase fraction, mean radius and number density. However, this assumption is a severe simplification since both, the volume and interface contributions to the nucleation free energy, are functions of temperature and size of the nucleus and the chemical composition of precipitate and matrix. To emphasize these dependencies, the symbols D_{f} and γ are introduced and used subsequently with

$$D_f = -\Delta G_{vol}\left(T, X_i\right) \tag{4}$$

where D_{f} denotes the driving force for the reaction and g the effective interface energy, given as

$$\gamma = \Delta G_{intf}\left(T, \rho, X_i\right) \tag{5}$$

In developing the Generalized Broken Bond (GBB) model, Sonderegger and Kozeschnik [26] utilize the direct relation between the specific interface energy and the solution enthalpy, ΔH_{sol}. In their treatment of the planar, sharp interface energy, γ_0, this quantity is written as

$$\gamma_0 = \frac{n_S \cdot z_{S,eff}}{N \cdot z_{L,eff}} \cdot \Delta H_{sol} \tag{6}$$

where n_{S} is the number of atoms on unit interfacial area and N is the Avogadro number. The quantities $z_{\mathrm{S,eff}}$ and $z_{\mathrm{L,eff}}$ are the effective number of broken bonds across the interface and the effective coordination number, respectively. The structural factor, $z_{S,eff}/z_{L,eff}$, is obtained, after averaging over several interfacial directions, with approximately 0.329 for fcc crystal structure and 0.328 for bcc.

In follow-up work, the same authors investigate the impact of interfacial curvature [27] and temperature [28] on the effective interface energy, of a small precipitate (nucleus), with the result that

$$\gamma = \alpha(\rho) \cdot \beta(T) \cdot \kappa \cdot \gamma_0\left(T, X_i\right) \tag{7}$$

where the functions $\alpha(\rho)$ and $\beta(T)$ are given as

$$\alpha(\rho) = 1 - \frac{20}{11}\cdot\frac{r_c}{\rho} + \left(\frac{45}{44} - \frac{1}{22}ln2\right)\cdot\left(\frac{r_c}{\rho}\right)^2 + \frac{1}{2}\cdot ln\left(\frac{\rho}{r_c}\right)\cdot\left(\frac{r_c}{\rho}\right)^2 \tag{8}$$

with $r_c = 0.3 \cdot r_1$, r_1 being the nearest neighbor atomic distance, and

$$\begin{aligned}\beta(T) \approx\ & 8.4729\cdot\left(\frac{T}{T_c}\right)^6 - 26.691\cdot\left(\frac{T}{T_c}\right)^5 + 32.717\cdot\left(\frac{T}{T_c}\right)^4 \\ & -17.674\cdot\left(\frac{T}{T_c}\right)^3 + 2.2673\cdot\left(\frac{T}{T_c}\right)^2 - 0.09\cdot \\ & \left(\frac{T}{T_c}\right) + 1.000476320\end{aligned} \tag{9}$$

and κbeing an efficiency factor for heterogeneous nucleation at particles such as dispersoids, which is discussed later in Section 2.4. Eq. (9) is a valuable polynomial fit to the implicit approximation published in ref. [28] and it is used in this form in the present analysis. With the regular solution critical temperature, T_{c} [28], the nucleus interface energy is unambiguously determined and used in Eq. (1) to compute the nucleation rate of a given precipitate as a function of the chemical alloy composition, temperature and cooling conditions.

2.3. Heterogeneous nucleation site energy

As indicated in the previous section, the effective interface energy, γ, can be predicted from thermodynamic information, i.e., CALPHAD-assessed Gibbs energies [29], and the alloy chemistry. Once this value enters the nucleation barrier expression, Eq. (3) together with the driving force, D_{f}, the nucleation barrier for homogeneous nucleation is well defined. However, this homogeneous nucleation value can be substantially altered when nucleation occurs at heterogeneous sites. The basic idea of considering the energetic conditions at heterogeneous sites is to assume that the nucleation event (i) replaces part of the heterogeneous site volume or area and (ii) can be facilitated by primary phases and dispersoids that offer surfaces with lower inter-phase boundary energy compared to that between the precipitate and the parent Al-matrix. With the associated energy gain / advantage at the heterogeneous nucleation site, ΔG_{het}, an extended nucleation energy expression can be written as

$$\Delta G_{nucl} = \frac{-4}{3}\pi\rho^3 \cdot D_f + 4\pi\rho^2 \cdot \gamma - \Delta G_{het}(\rho) \tag{10}$$

In contrast to the CNT treatment, the critical nucleation energy and the critical radius can no longer be evaluated as a closed analytical expression but must be sought by numerical techniques.

The reduction of the effective nucleation barrier at heterogeneous sites makes the nucleation event energetically more favorable than the homogeneous case. The amount of this gain in energy by removing,

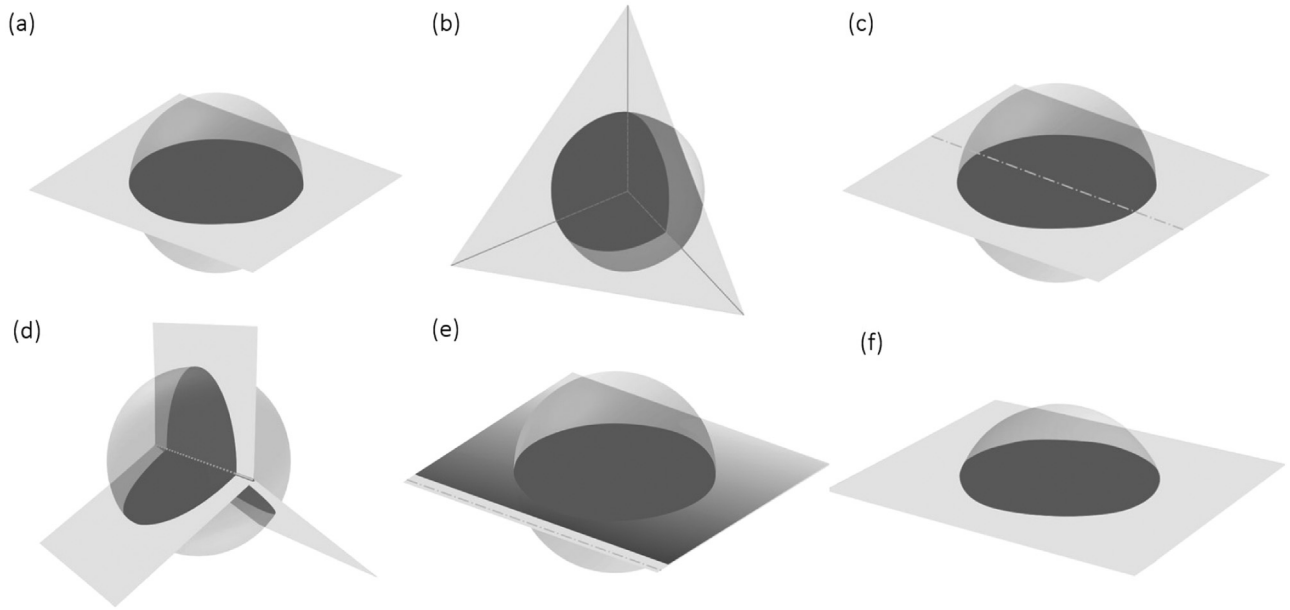

Fig. 1. Heterogeneous nucleation sites: (a) grain boundary, (b) grain boundary corner, (c) dislocation, (d) grain boundary edge, (e) stress field of the dislocation and (f) epitaxial on particle surface.

Table 1
Energies of structural heterogeneous nucleation sites. ρ … radius of the nucleus, γgb … grain boundary energy, L … dislocation line energy.

Bulk	Dislocation	Grain boundary	GB edge	GB corner	2nd-phase particle
0	$\eta \cdot \rho G b^2$	$\pi\rho^2\gamma_{\mathrm{gb}}$	$3/2\ \pi\rho^2\ \gamma_{\mathrm{gb}}$	$6\ \arctan(\sqrt{2})\ \rho^2\ \gamma_{\mathrm{gb}}$	$2\kappa_s \cdot \pi\rho^2\gamma_{gb}$

e.g., grain boundary or dispersoid/matrix interfacial area, must be interpreted in relation to the available driving force for precipitate formation. When the driving forces are small, the gain in energy can be comparably large and even over-compensate the homogeneous nucleation barrier, which means that the nucleation barrier vanishes. Barrier-free nucleation has also been proposed by van Dijk et al. [30] for the austenite to ferrite transformation in steel or by Song and Hoyt [31] in molecular dynamics simulations. Fig. 1 shows a sketch of possible heterogeneous nucleation sites for a spherical nucleus, whereby Fig. 1(c) depicts nucleation directly on a dislocation line and Fig. 1(e) shows nucleation at the stress field next to the dislocation (color gradient). Dark grey planes in the figure indicate the respective interfacial areas.

The calculation of ΔG_{het} for various nucleation sites involving planar or linear lattice defects (grain boundaries and dislocations) is based on purely geometrical considerations. The associated equations are summarized in Table 1. For nucleation on grain boundaries (GB), grain boundary edges (GBE) and corners (GBC), the gain in energy is related to the removal of a certain amount of grain boundary area by the volume of the newly formed precipitate. In the case of dislocations, the energy advantage is associated with the partial removal of the dislocation stress field described by the dislocation line energy, L, which is, in a first approximation, related to one half of the shear modulus, G, and the square of the Burgers vector, b, with $L=0.5Gb^2$ [32]. Since the nucleus of a new phase usually does not remove the crystal defect represented by a dislocation but rather relax either the compressive or tensile part of the dislocation stress field, the maximal amount of energy gain given by the product of nucleus diameter, $2r$, and dislocation line energy, L, might be weighted by an efficiency factor, $\eta \leq 1$, which is an a-priori unknown calibration coefficient in the practical calculation.

Like in the case of the dislocation stress field, heterogeneous nucleation at particles is difficult to predict on a rigorous basis. Some treatments based on geometrical considerations for the nucleus shape are reported, e.g., in refs. [33–35]. Since several input quantities in the rigorous treatments are commonly unknown, in the approximation taken in the present work, it is assumed that this type of heterogeneous nucleation site can be accounted for by (i) a calibration factor, $\kappa_{\mathrm{i}} \leq 1$, for the effective (average) interface energy representing the chemical contribution to the interface energy at a coherent phase boundary (Eq. (7)) and (ii) an additional structural (incoherent) energy contribution resulting from modification of the original phase boundary structure to an energetically more favorable new interface structure. This energy contribution is assumed to be maximally in the order of the grain boundary energy of the Al-matrix. It is, therefore, related to this quantity by a further calibration factor, $\kappa_{\mathrm{s}} \geq 0$, representing the contribution to the heterogeneous site energy given by the difference in structural energy of the original incoherent interfacial area at the 2$^{\mathrm{nd}}$-phase particle compared to the newly formed interface between particle and nucleus. The factor 2 in the expression listed in Table 1 is introduced for convenience, mostly accounting for the fact that the half-cap nucleus is assumed to be in contact with the particle surface in an angle smaller than 90° and the new phase can be approximated by a spherical cap instead of a full half-sphere. It is further assumed that the particles are sufficiently large compared to the critical nucleus size to offer a nearly planar heterogeneous nucleation surface.

Depending on the particular energetic constitution of the interface between a particle and a new nucleus and the strength of chemical and structural contributions, particles often represent most favorable nucleation sites in metallic microstructures. For the case of the 6005 alloy investigated here, the preferred heterogeneous nucleation sites are AlFeMnSi-primary phases for β-Mg_2Si [17,20,22] and Al(Cr,Mn,Fe)Si-dispersoids for B'-$Al_4Mg_8Si_7$ [17,20,36]. It should be mentioned that various additional nucleation mechanism for aluminium based alloys were documented in literature e.g. dislocations as nucleation sites in binary Al-Si or ternary Al-Mg-Si alloys [20,37].

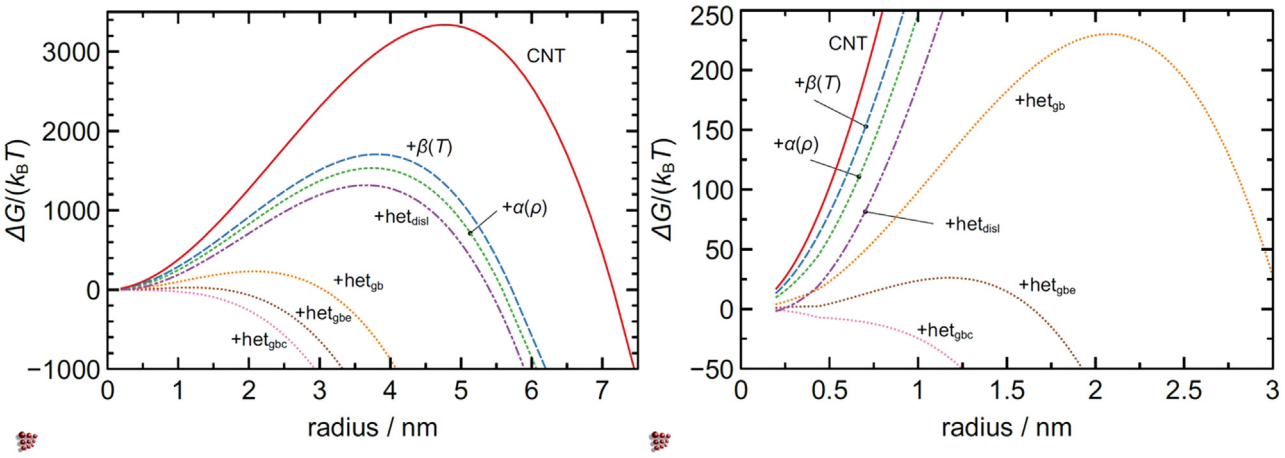

Fig. 2. Nucleation energy of β-Mg2Si at 500 C as a function of the precipitate radius and a grain boundary energy, $\gamma_{gb} = 0.5 J/m^2$. CNT… classical nucleation theory; with the effects of $\beta(T)$… diffuse interface, $\alpha(\rho)$… interface energy size effect, and heterogeneous nucleation energy with hetdisl … dislocation, hetgb … grain boundary, hetgbe … grain boundary edge and hetgbc … grain boundary corner. The right image is a close-up for heterogeneous energy contributions.

Table 2
Mass fractions of alloying element atoms [ma. %]. The bold elements are considered in the thermokinetic simulations.

Alloy	Si	Fe	Cu	Mn	Mg	Cr	Zn	Ti
AA6005A	0.68	0.2	0.01	0.11	0.57	0.04	0.01	0.018

2.4. Thermodynamic analysis of the nucleation barrier

This section discusses several theoretical scenarios for the computed precipitate nucleation barrier based on β-Mg_2Si. The mass fractions of alloying element atoms of the studied Al-alloy are summarized in Table 2. Only the ternary Al-Mg-Si system is considered in the thermodynamic and precipitation kinetics simulations for the benefit of clear interpretation. Thermodynamic equilibrium calculations based on the open-source database "mc_al.tdb", version 2.035 (from http://matcalc.at), indicate that the solvus of the β-Mg_2Si phase is shifted to a lower temperature by less than 2 K when ignoring the trace elements. The direct thermodynamic influence on β-Mg_2Si and B'-$Al_4Mg_8Si_7$ precipitates can thus be neglected. Kinetic considerations to this simplification are elaborated later in Section 3.1.

Fig. 2 displays the normalized nucleation energy of the stable β-Mg_2Si phase evaluated with Eq. (10) as a function of the precipitate radius at a temperature of 500°C, which is roughly 25 K below the thermodynamic solvus of 528°C. The grain boundary energy, γ_{gb}, has been reported to be an effective quantity with an average value between 0.3 - 0.5 J/m^2 [38–40]. Here, a grain boundary energy, $\gamma_{gb} = 0.5 J/m^2$, is used unless stated otherwise. The solid lines labeled with "CNT" correspond to the evaluation of ΔG_{nucl} by employing Eq. (10) for constant values of D_f and γ and in the absence of the heterogeneous nucleation site energy, ΔG_{het}. The diagram also shows the shape of the nucleation energy versus radius curve when contributions of different mechanisms, which lead to a reduction of the effective precipitate/matrix interface energy and, consequently, a reduced nucleation barrier, are considered. These are the diffuse interface effect [41] (dashed blue lines) and the interface energy size effect [27] (light dashed green lines). These two contributions have also been considered in simulations performed in previous work [14,15].

The temperature of 500°C is chosen for the computational analysis in Fig. 2 because it corresponds roughly to the temperature where the first DSC signal is observed in the experiments with lowest cooling rate (see Section 4, later). Interestingly, the predictions of CNT (solid lines) indicate that the nucleation of the stable equilibrium phase β-Mg_2Si should be entirely suppressed because the nucleation barrier adopts a value of more than 3000 k_BT. This value delivers practically zero for the exponential term in Eq. (1) and, consequently, a nucleation rate that is almost zero. Even when considering the diffuse interface effect with the parameter $\beta(T)$ and the interface energy size effect with α(ρ), the nucleation barrier is still too high for any conceivable precipitation with barrier values of roughly 1500 k_BT.

A large effect in terms of a nucleation barrier reduction stems from the heterogeneous nucleation site energy, i.e., grain boundaries and the corresponding edges and corners. Assuming a grain boundary energy value of 0.5 J/m^2, the nucleation barrier at grain boundary faces and edges adopt values of approximately 230 k_BT, and 26 k_BT, respectively. In practical terms, these values are still too high for conceivable nucleation. For instance, the exponential term in the nucleation rate expression, Eq. (1), is $5.1 \cdot 10^{-12}$ at grain boundary edges. In contrast, the energy gain in nucleation at grain boundary corners is high enough to compensate the energy expense of the newly formed precipitate/matrix interface. The close-up for heterogeneous nucleation sites in the right image of Fig. 2 shows that the nucleation energy is negative from the beginning. Nucleation at grain boundary corners is, therefore, energetically advantageous from the beginning and it occurs spontaneously without any nucleation barrier below a characteristic temperature, in accordance with the experimental evidence presented later in Section 4. The outstanding role of grain boundary corners has also been emphasized, e.g. by Huang and Hillert [42] in an investigation of the austenite to ferrite transformation in steel, where the authors observe that proeutectoid ferrite nucleation occurs almost exclusively on these heterogeneous nucleation sites and that it is practically absent elsewhere in the microstructure.

Fig. 3 displays the computed nucleation energy at grain boundary corners for various temperatures in the vicinity of the β-Mg_2Si solvus (528°C) when assuming a grain boundary energy value of 0.5 J/m^2. According to this analysis, first conceivable nucleation of β-Mg_2Si at grain boundary corners should occur below roughly 510°C, where the nucleation barrier is evaluated with 4 k_BT, and the exponential term adopts a value of around $1.8 \cdot 10^{-2}$.

The method of evaluating the nucleation barrier in the presence of heterogeneous nucleation site energies is sketched for the temperature of 512°C in the close-up diagram of Fig. 3. Up to a radius of roughly 0.4 nm, the nucleation energy decreases. This indicates that formation of a nucleus up to this size is energetically favorable in any instance and will occur spontaneously. A nucleus of this size contains approximately ten atoms. Above this size, the nucleation energy increases again and forms a nucleation barrier that is evaluated as the difference between

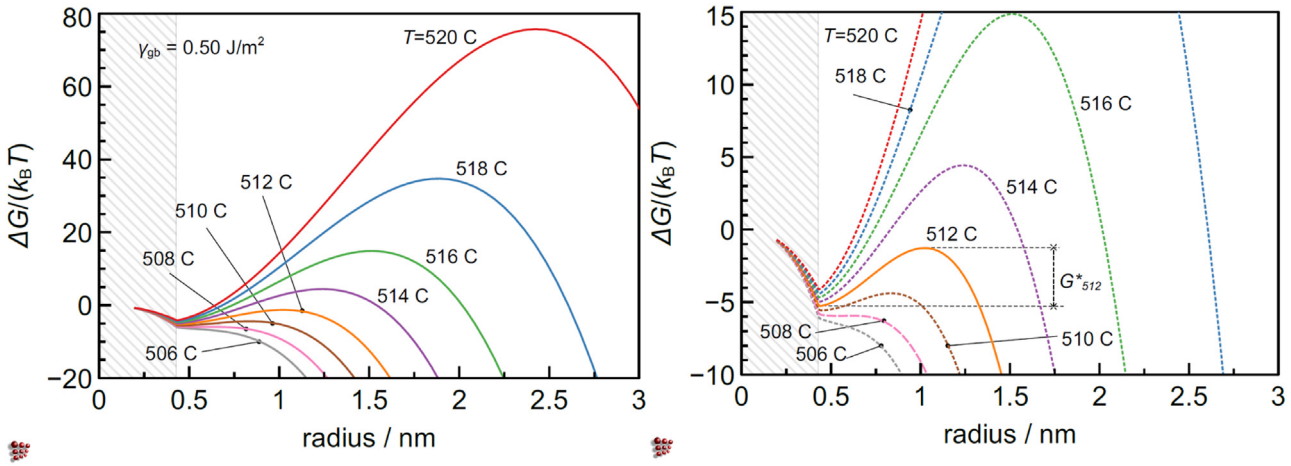

Fig. 3. Calculated nucleation energy, ΔG, for β-Mg2Si precipitation at grain boundary corners for various temperatures.

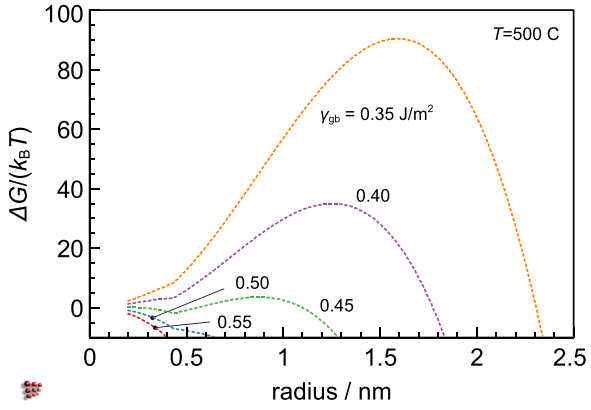

Fig. 4. Calculated nucleation energy, G, for β-Mg2Si precipitation at grain boundary corners at 500 C for various values of the grain boundary energy, γgb.

the minimum at around 0.4 nm and the maximum of the nucleation energy after the subsequent increase of nucleus size. The corresponding quantity is denoted as "G^*_{512}" in Fig. 3. At around 508°C and below, the nucleation barrier vanishes completely. In this case, the gain of energy due to the removal of grain boundary area is always larger than the energy expense for the formation of new precipitate/ matrix interfacial area. Note that the shaded areas in Fig. 3 denote regions, which are outside the validity limits of the models for the interface energy size [27] and diffuse interface effects [41]. The discontinuity in the curves is also due to this limit.

Fig. 4 shows the calculated grain boundary corner nucleation free energy at 500°C for different values of the grain boundary energy. When using a value, which is located at the lower end of the reported values, i.e., 0.35 J/m^2 [38,43], the nucleation barrier is roughly 90 $k_B T$, with 0.45 J/m^2, it is close to 7 $k_B T$. At a value of 0.5 J/m^2, which is a value that is on the higher end of reported values [40], the nucleation barrier vanishes.

Fig. 5 summarizes some relevant nucleation parameters for β-Mg_2Si precipitation, both for homogeneous nucleation (solid lines) and at heterogeneous sites, such as dislocations (dotted lines), grain boundary faces (dashed lines), edges (dash-dotted lines) and corners (dash-dot-dotted lines). The left plot column shows calculated values for the critical nucleation energy, G^*, the critical radius, r_{crit}, and the steady-state nucleation rate, J, Eq. (1) without the exponential term for the incubation time, for a grain boundary energy of $\gamma_{gb} = 0.35$ J/m^2. The right column shows the same quantities for a value of 0.5 J/m^2. The driving force for β-Mg_2Si precipitation is shown in Fig. 6.

The top left plot in Fig. 5 displaying the normalized critical nucleation energy, i.e., the nucleation barrier, indicates that heterogeneous site energies substantially reduce the effective barrier energy. The solid line shows that the barrier for homogeneous nucleation conditions remains at rather high values even at temperatures as low as 300°C, where the barrier is roughly 20 $k_B T$. In contrast, at grain boundaries, the nucleation barrier disappears below approximately 335°C, which is the temperature where the energy expense in creating new precipitate/matrix interface is fully compensated by the energy gain accompanying the removal of grain boundary area. At grain boundary corners, this situation is encountered already at 450°C. When assuming a grain boundary energy of $\gamma_{gb} = 0.5$ J/m^2 (right plot column), similar predictions are obtained, however, the transition temperatures, where barrier-less nucleation occurs, are shifted to substantially higher values.

The calculated critical nucleation energies in the top left plot shows an interesting feature. The lines for nucleation at grain boundaries and dislocations cross over at approximately 390°C. This feature is caused by the different geometries that are suggested by the removal of defect volume, which is related to the square of the precipitate radius in the case of planar defects and two times the precipitate radius in the case of linear defects.

The two bottom plots in Fig. 5 display the steady-state nucleation rates corresponding to the values of the critical nucleation energy. After an initial increase of the nucleation rate with decreasing temperature, the values reach a maximum, which corresponds to the points where all potential nucleation sites are occupied. The continuous decrease after reaching this peak value is due to decreasing diffusivities, which are incorporated in the atomic attachment rate, β^*, in Eq. (1). Further details for calculation of nucleation rates are given, e.g., in ref. [25].

Finally, a parameter study for heterogeneous nucleation at dispersoid and primary particles is performed in the present context, showing limiting cases for $K_s = 0$ and hypothetical $K_s = 1$. As mentioned above, these phases act as main nucleation sites in common aluminium 6xxx alloys. The two parameters entering the simulation are the calibration factor for the effective interface energy, K_i, and the calibration factor for the structural energy contribution, K_s. The latter quantity is held constant with either $K_s = 0$, which corresponds to the situation where the original and new interfacial areas have the same structural energy contribution or with $K_s = 1$, which corresponds to the hypothetical situation where the originally incoherent dispersoid/matrix interface is replaced by a coherent dispersoid/precipitate interface (Fig. 7) and the nucleation barrier is reduced by the term given in Table 1.

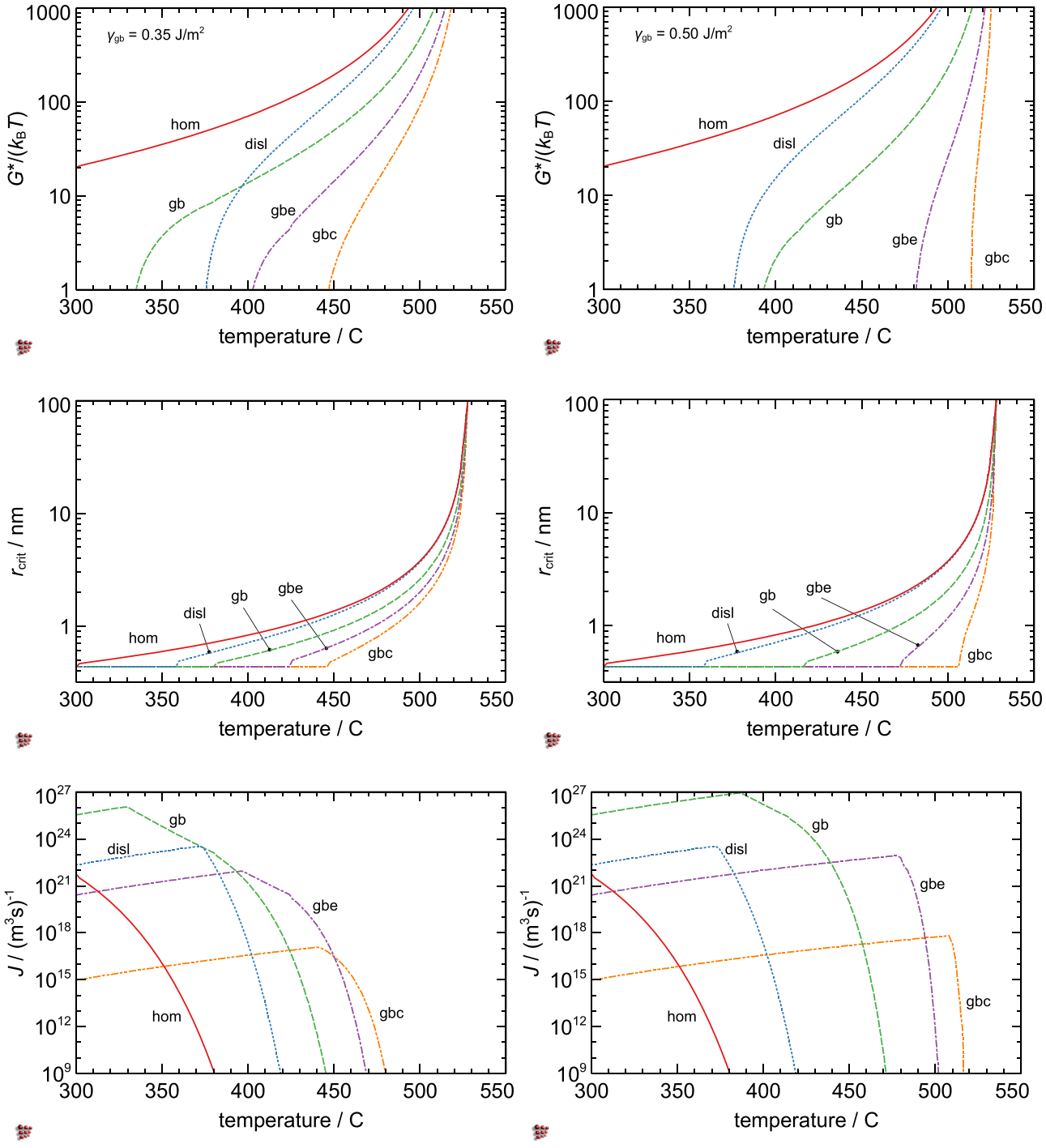

Fig. 5. Calculated critical nucleation energy, G*, critical radius, rcrit, and steady-state nucleation rate, J, for β-Mg2Si precipitation as function of temperature for two values of the grain boundary energy, γ_{gb}. Nucleation at grain boundary corners (dash-dot-dotted lines), edges (dash-dotted lines), faces (dashed lines), dislocations (dotted lines) and homogeneously (solid lines).

The reduction of the chemical contribution to the interface energy that is required to facilitate nucleation under conditions of low driving force is substantial, if the amount of structural energy contribution between old and new dispersoid/primary precipitate interface is the same in the nucleation process. The left plot in Fig. 7, representing the limiting case where the structural energy contribution during nucleation remains unchanged, indicates that the scaled nucleation barrier reaches values close to unity, i.e. substantial nucleation rates, only if the effective interface energy is reduced to roughly 15 % of the predicted interface energy value between matrix and precipitate. On the other hand, if an initially incoherent interface, comprising chemical and structural energies of the interface, were replaced by a coherent interface, the required reduction of the chemical contribution is predicted to be roughly around 67 %. The simulation suggests that heterogeneous nucleation at dispersoids/primary phases most likely involves both, contributions from the change of structural interface energy as well as a reduction of the chemical contribution of the interface energy. How much the contributions of the two mechanisms during epitaxial nucleation on the nucleation barrier are, is not further elaborated here and remains to be estimated for each nucleation case individually by an appropriate choice

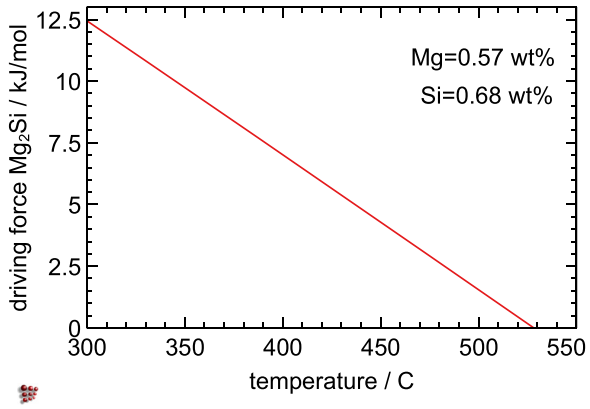

Fig. 6. Calculated chemical driving force for β-Mg2Si precipitation as a function of temperature.

for the parameters K_i and K_s. In the simulations shown subsequently, the structural energy contributions, K_s for the B' and β-Mg_2Si precipitates is chosen as 0.3 and 0.25, respectively. The parameters describing the assumed reduction of interfacial energy between nucleus and primary precipitate, as 0.4 and 0.5, respectively.

2.5. Calculation of excess specific heat capacities

The excess specific heat capacity Δc_p is a convenient thermodynamic quantity for comparing computational simulation results with experimental calorimetric data [14]. Δc_p represents the heat flow difference of a sample $\dot{Q}_s$ and an inert reference with identical basic absolute heat capacity $\dot{Q}_{ref}$ divided by the sample mass, m_p, and the cooling rate $\dot{T}$ with

$$\Delta c_p = \frac{\dot{Q}_s - \dot{Q}_{ref}}{m_p \dot{T}} \tag{11}$$

The simulations deliver Calphad-based specific enthalpies, H_s, that are evaluated in the scope of the precipitation simulation during each computation increment. Consequently, one can directly use H_s from the simulations to obtain the expression for Δc_p as

$$\Delta c_p = \frac{d\left(H_s - H_{ref}\right)}{dT} \tag{12}$$

where H_{ref} is the enthalpy of a reference alloy matrix phase, which has the same composition as the reference sample in the DSC-measurement.

The two expressions for Δc_p, Eqs. (11) and (12), allow for a consistent comparison between experiment and simulation.

3. Thermokinetic simulation

The MatCalc software package [44] is used for the precipitation kinetics simulations in this study, with assessed CALPHAD descriptions of Al-base matrix and precipitates [9]. For the simulations, the open thermodynamic databases "mc_al.tdb", version 2.035, and the open diffusion database "mc_al.ddb", version 2.004 are used. Thermokinetic simulations of precipitation during continuous cooling are performed and simulated excess c_p values are compared with calorimetric data from various DSC cooling experiments. The primary experimental data is adopted from Milkereit et al. [17,45], who performed DSC cooling experiments in AA6xxx alloys for various cooling rates combined with microstructural characterization of grain size and microanalysis of precipitated phases as well as their preferential heterogeneous nucleation sites.

3.1. Input data for simulation

The chemical composition of the alloy used in the experiments is summarized in . In the simulations, the ternary Al-Mg-Si system is considered for the merit of easy interpretation. The trace elements Fe, Cu, Mn, Cr, Zn and Ti form intermetallic compounds (dispersoids), which are beneficial in controlling grain size but do not take part in the reactions visible in the continuous cooling DSC experiments. They are accounted for in the simulations in an indirect way since they provide heterogeneous nucleation sites for the epitaxial nucleation of B' precipitates as well as for the β-Mg_2Si-phase. The effective number densities of dispersoids and primary phases are treated as calibration coefficients in the present simulation, due to insufficient experimental information. The dispersoid distribution is practically not altered in the DSC test [46,47]. The same can also be assumed for primary phases, which act as nucleation sites for β-Mg_2Si-particles. Table 3 summarizes all input data and parameters for simulation.

In analogy to the experiments, the heat treatment [17,45] for the simulations consists of a solution treatment at 540°C for 20 min, followed by cooling to room temperature with different cooling rates from 0.00167 K/s up to 6.25 K/s. The experiments show that, during cooling, the β-Mg_2Si-phase forms at higher temperatures around 500-350°C, whereas the B'-phase precipitates at intermediate temperatures between 350 and 200°C. The β-Mg_2Si-phase mostly nucleates at coarse primary phases. The B'-phase is consistently attached to Al(Cr,Mn,Fe)Si dispersoids, which form during the homogenization heat treatment at tem-

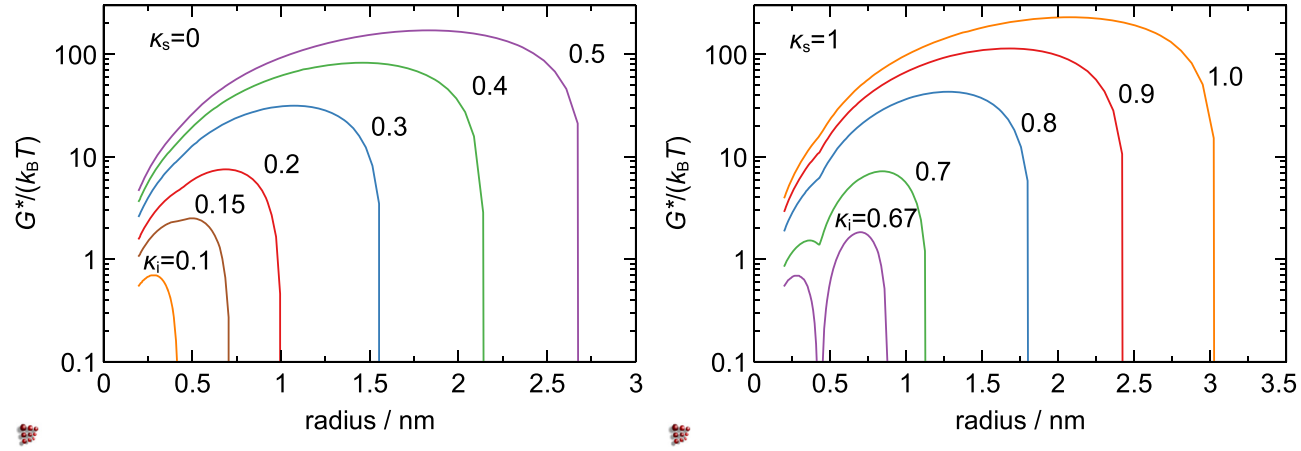

Fig. 7. Energy barrier at 500°C for nucleation at dispersoid particle surfaces in dependence of the efficiency factor K_i for the limiting cases of $K_s = 0$ (left plot, no structural energy contribution change during nucleation) and $K_s = 1$ (right plot, hypothetical case where an incoherent original interface is replaced by a coherent one). The precipitate size and diffuse interface effects are accounted for in the simulation.

Table 3
Input data for precipitation simulation.

Input parameter	Value	Reference
T_{crit} β-Mg_2Si phase	1950 K	[41]
T_{crit} B'-$Al_4Mg_8Si_7$ phase	1520 K	[41]
Heterogeneous interface energy factors, K_I/K_s, for B'-$Al_4Mg_8Si_7$ phase	0.4 / 0.3	This work
Heterogeneous interface energy factors, K_I/K_s, for β-Mg_2Si phase	0.5 / 0.25	This work
Number density of dispersoids for epitaxial nucleation	$2{\cdot}10^{19}$	[1]
Number density of primary phases for epitaxial nucleation	$1{\cdot}10^{15}$	This work

peratures above around 350°C [48]. Since the final distribution of dispersoids becomes stationary during the solution heat treatment before continuous cooling, a constant number of dispersoids is deemed to prevail during the DSC experiments, thus supporting the assumption of a constant number of potential nucleation sites for the B'-phase in the simulations. It is further assumed that the B'-phase nucleates epitaxially at the dispersoid surfaces because of a reduction of heterogeneous interface energy and/or replacement of incoherent interfacial area by coherent/semi-coherent interfaces compared to homogeneous nucleation in the bulk. In the simulation, this effect is accounted for by a decrease of the overall effective interface energy with a factor 0.4 and a structural contribution with $k_s = 0.3$ (see also previous discussion of Fig. 7). Since there exists no reliable experimental data on the number density of dispersoids, the density is only estimated for the given alloy composition based on a work of Strobel et al. [1]. Also a dependence of dispersoid particle density on chemical composition of the alloy is reported [23]. Similar assumptions are made for the β-Mg_2Si-phase, where values of $K_i = 0.5$ and $K_s = 0.25$ are used. Moreover, of cause the particularly applied homogenization treatment at which the dispersoids formed might influence on the dispersoids particle density [23].

The regular solution critical temperatures, T_{crit}, for the B'-$Al_4Mg_8Si_7$ and β-Mg_2Si-phases in the diffuse-interface model [41], are summarized in are Table 3. They are evaluated in accordance with the procedure outlined in ref. [25].

3.2. Analysis of peak temperature and area below the curves

Numerous methods are reported to properly evaluate the area under a DSC curve, see, e.g. Milkereit [45]. The total heat generation during an exothermic phase transformation can be extracted by methods, such as "fitting the curve with Gauss-functions" or "stepwise peak integration". Each of these methods is characterized by certain advantages and disadvantages. In the present study, "stepwise peak integration" as presented in Fig. 2 of [19] is used for the calculation of peak areas, where the area under the DSC-curves correlates to the intensity of the reaction or the volume fraction of precipitated phases. Furthermore, from analysis of peak temperatures of excess c_p, information on the nucleation behavior of phases can be extracted.

4. Results

Fig. 8 shows the comparison of thermokinetic simulations with the experimental data for cooling rates from 0.00167 to 1.67 K/s obtained from the continuous cooling DSC experiments for the AA6005A alloy. According to Milkereit [17], the first peak at higher temperatures is associated with the precipitation of β-Mg_2Si-phase and the second peak at lower temperatures with the precipitation of B'- $Al_4Mg_8Si_7$ phase. The β-Mg_2Si-phase peak marks the dominant reaction at slow (0.00167 – 0.0167 K/s) cooling rates. It disappears gradually with increasing cooling rates and the peak temperature is slightly shifted to lower temperatures. In contrast, the B'- $Al_4Mg_8Si_7$ phase reaction first intensifies with increasing (0.0167 – 0.5 K/s) cooling rates and is shifted to higher temperatures. This shift appears simultaneously to the fading (i.e., gradual kinetic suppression) of the β-Mg_2Si phase precipitation. During cooling at 1.67 K/s precipitation of β-Mg_2Si seems to be fully suppressed while

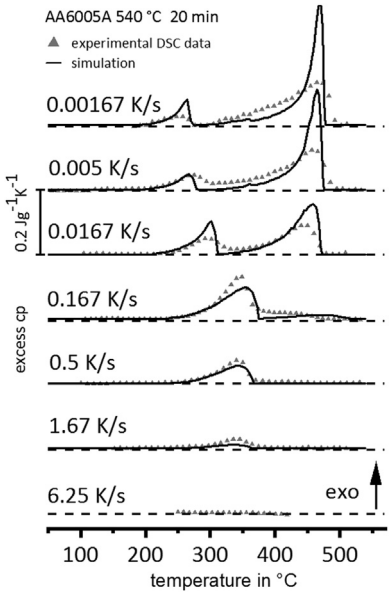

Fig. 8. Comparison of experimental data and simulation - the solid lines represent simulation results and symbols denote experimental DSC data.

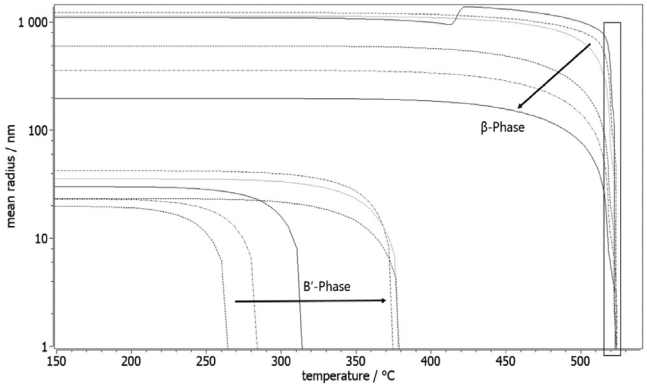

Fig. 9. Evolution of Mg-Si-phase radii depending on cooling rate.

at the highest cooling rate of 6.25 K/s, no precipitation reaction occurs anymore. Table 4 provides detailed information about peak temperatures excess c_p and the reaction intensity in the form of the integrated peak areas comparing experimental and simulated curves. In comparison to experimental data, simulation shows no peak overlapping. Therefore, integration limits are automatically determined by the intensity signal, which drops to zero between the first and the second reaction. For each cooling rate, the deviation in peak temperatures and area is given via a temperature difference or percentage value referring to the experimental data as reference.

To get the connection between the simulations of excess c_p and precipitate evolution, Figs. 9 and 10 give a detailed view on the develop-

Table 4
Detailed comparison of peak temperatures and peak area – identical simulation parameter set for all cooling rates.

	β-Mg_2Si phase				B'-$Al_4Mg_8Si_7$ phase			
Cooling rate [K/s]	temperature [C]			peak area [%]	temperature [C]			peak area [%]
	exp	sim	ΔT		exp	Sim	ΔT	
0.00167	468	470	2	98	250	264	14	170
0.005	459	466	7	105	273	267	6	58
0.0167	444	458	14	126	294	301	7	121
0.167	391	470	79	89	345	354	9	85
0.5	-	-	-	-	343	344	1	71
1.67	-	-	-	-	340	338	2	36

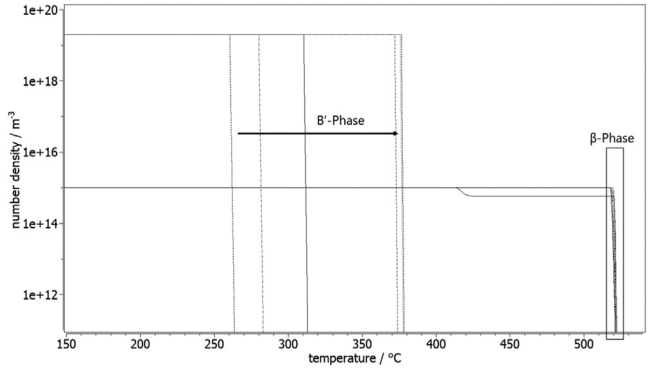

Fig. 10. Evolution of Mg-Si-phase number density depending on cooling rate.

ment of mean precipitate radius as well as number density depending on cooling rate. The arrows in the figures indicate the evolution of mean radius and number density from slow (0.00167 K/s) to high (1.67 K/s) cooling rates. β-Mg_2Si phase shows a reduction of mean radius with higher cooling rates due to the reduced time that is available for precipitate growth. In comparison, the mean radius of B'-$Al_4Mg_8Si_7$ phase increases with cooling rates, attributable to the higher amount of solutes available to form the precipitates. Fig. 10 shows that soon after the onset of nucleation, practically all preferred heterogeneous nucleation sites are occupied, and nucleation is stopped (nucleation site saturation). It is also evident that the nucleation start temperature of B'-$Al_4Mg_8Si_7$ is shifted to higher temperatures with higher cooling rates. Nucleation of β-Mg_2Si phase occurs in a narrow temperature window of 10 K. In addition, experimental data show a sharp increase in excess specific heat capacity, which indicates a simultaneous nucleation of the β-Mg_2Si precipitates, which is in good accordance with the simulation trends.

It is emphasized that all simulations are performed with a single identical set of input parameters for all cooling rates. When analyzing the correlation between experiments and simulation results for the calculations for all cooling rates, the accordance is exceptionally good. Regarding the peak temperatures, experimental and simulation values are in excellent agreement, with a maximum deviation of 14 K (3.5 %). The only (possible) outlier is identified for the β- Mg_2Si peak at a cooling rate of 0.167 K/s, where the difference between measured and calculated peak value is larger than 70 K. However, the experimental peak is characterized by rather low intensity of the β-Mg_2Si phase precipitation signal, and no distinct peak associated to the β-Mg_2Si reaction is visible. Instead, a smooth transition to the precipitation reaction of the B'-$Al_4Mg_8Si_7$ phase is observed, making a precise evaluation of the peak temperature for experimental data challenging. A reproduction of the experimental β-Mg_2Si phase precipitation peak for this cooling rate cannot be improved without deteriorating the good agreement at other cooling rates. In the simulation, the calculated peak area for the β-Mg_2Si phase is narrower and higher as compared to experiments. This is attributed to experimental conditions, where material in homogeneities provide heterogeneous nucleation sites with a variety of energies, whereas the simulations are performed for idealized nucleation sites with only one single value for heterogeneous nucleation site energies. Comparisons with other aluminium based alloys are subject of ongoing work. For this, additional effects in thermo-kinetic simulation must be considered like the influence of cooling rate on morphology characteristics of certain phases [20].

6. Summary

In the present work, an extended formulation for the nucleation energy in the presence of heterogeneous nucleation sites is developed and applied to the prediction of DSC curves during continuous cooling experiments. The present model accounts for nucleation conditions at dislocations as well as grain boundary faces, edges, and corners. Heterogeneous, epitaxial nucleation on particles is accounted for with two calibration factors for the effective overall interface energy reduction as well as the (partial) substitution of incoherent interfacial area by coherent/semi-coherent one. It is demonstrated that the experimentally observed precipitation kinetics is well described if the energy gain accompanying the heterogeneous nucleation event is properly considered while the simulation entirely fails if the impact of heterogeneous sites is neglected.

Declaration of Competing Interest

The authors declare that they have no known competing financial interests or personal relationships that could have appeared to influence the work reported in this paper.

Acknowledgment

The financial support by the Austrian Federal Ministry for Digital and Economic Affairs and the National Foundation for Research, Technology and Development is gratefully acknowledged.

References

[1] K. Strobel, M.A. Easton, L. Sweet, M.J. Couper, J.F. Nie, Relating quench sensitivity to microstructure in 6000 series aluminium alloys, Mater. Trans. 52 (2011) 914–919, doi:10.2320/matertrans.L-MZ201111.
[2] Y. Sun, D.R. Johnson, K.P. Trumble, P. Priya, M.J.M. Krane, Effect of Mg2Si Phase on Extrusion of AA6005 Aluminum Alloy, Light Met 2014 (2014) 429–433 9781118889, doi:10.1002/9781118888438.ch73.
[3] K. Strobel, M.D.H. Lay, M.A. Easton, L. Sweet, S. Zhu, N.C. Parson, A.J. Hill, Effects of quench rate and natural ageing on the age hardening behaviour of aluminium alloy AA6060, Mater. Charact. 111 (2016) 43–52, doi:10.1016/j.matchar.2015.11.009.
[4] Y. Birol, Homogenization of en AW 6005A Alloy for Improved Extrudability, Metall. Mater. Trans. A Phys. Metall. Mater. Sci. 44 (2013) 504–511, doi:10.1007/s11661-012-1379-y.
[5] S. Zajac, B. Bengtsson, C. Jönsson, Influence of cooling after homogenisation and reheating to extrusion on extrudability and final properties of AA 6063 and AA6082 alloys, Mater. Sci. Forum. 396 (2002) 399–404 –402, doi:10.4028/www.scientific.net/msf.396-402.399.
[6] G. Mrówka-Nowotnik, J. Sieniawski, Influence of heat treatment on the microstructure and mechanical properties of 6005 and 6082 aluminium alloys, J. Mater. Process. Technol. 162 (2005) 367–372 –163, doi:10.1016/j.jmatprotec.2005.02.115.
[7] Y. Ohmori, L.C. Doan, Y. Matsuura, S. Kobayashi, K. Nakai, Morphology and crystallography of β-Mg2Si precipitation in Al-Mg-Si alloys, Mater. Trans. 42 (2001) 2576–2583, doi:10.2320/matertrans.42.2576.

[8] S.D. Dumolt, J.C. Laughlin, D. E.Williams, Formation of β' phase in aluminum alloy 6061, Scr. Metall. 18 (1984) 1347–1350.

[9] E. Povoden-Karadeniz, P. Lang, P. Warczok, A. Falahati, W.W.W. Jun, E. Kozeschnik, CALPHAD modeling of metastable phases in the Al-Mg-Si system, Calphad Comput. Coupling Phase Diagrams Thermochem. 43 (2013) 94–104, doi:10.1016/j.calphad.2013.03.004.

[10] S. Esmaeili, X. Wang, D.J. Lloyd, W.J. Poole, On the precipitation-hardening behavior of the Al-Mg-Si-Cu alloy AA6111, Metall. Mater. Trans. A Phys. Metall. Mater. Sci. 34 (2003) 751–763, doi:10.1007/s11661-003-1003-2.

[11] M.J. Starink, Analysis of aluminium based alloys by calorimetry: Quantitative analysis of reactions and reaction kinetics, Int. Mater. Rev. 49 (2004) 191–226, doi:10.1179/095066004225010532.

[12] Y. Birol, DSC analysis of the precipitation reaction in AA6005 alloy, J. Therm. Anal. Calorim. 93 (2008) 977–981, doi:10.1007/s10973-007-8686-3.

[13] A. Gaber, A.M. Ali, K. Matsuda, T. Kawabata, T. Yamazaki, S. Ikeno, Study of the developed precipitates in Al-0.63Mg-0.37Si-0.5Cu (wt.%) alloy by using DSC and TEM techniques, J. Alloys Compd. 432 (2007) 149–155, doi:10.1016/j.jallcom.2006.06.004.

[14] P. Lang, T. Wojcik, E. Povoden-Karadeniz, A. Falahati, E. Kozeschnik, Thermokinetic prediction of metastable and stable phase precipitation in Al-Zn-Mg series aluminium alloys during non-isothermal DSC analysis, J. Alloys Compd. 609 (2014), doi:10.1016/j.jallcom.2014.04.119.

[15] P. Lang, E. Povoden-Karadeniz, A. Falahati, E. Kozeschnik, Simulation of the effect of composition on the precipitation in 6xxx Al alloys during continuous-heating DSC, J. Alloys Compd. (2014) 612, doi:10.1016/j.jallcom.2014.05.191.

[16] A. Falahati, E. Povoden-Karadeniz, P. Lang, P. Warczok, E. Kozeschnik, Thermokinetic computer simulation of differential scanning calorimetry curves of AlMgSi alloys, Int. J. Mater. Res. 101 (2010) 1089–1096, doi:10.3139/146.110396.

[17] B. Milkereit, N. Wanderka, C. Schick, O. Kessler, Continuous cooling precipitation diagrams of Al-Mg-Si alloys, Mater. Sci. Eng. A. 550 (2012) 87–96, doi:10.1016/j.msea.2012.04.033.

[18] B. Milkereit, O. Kessler, C. Schick, Recording of continuous cooling precipitation diagrams of aluminium alloys, Thermochim. Acta. 492 (2009) 73–78, doi:10.1016/j.tca.2009.01.027.

[19] B. Milkereit, M.J. Starink, Quench sensitivity of Al-Mg-Si alloys: A model for linear cooling and strengthening, Mater. Des. 76 (2015) 117–129, doi:10.1016/j.matdes.2015.03.055.

[20] B. Milkereit, M.J. Starink, P.A. Rometsch, C. Schick, O. Kessler, Review of the quench sensitivity of aluminium alloys: Analysis of the kinetics and nature of quench-induced precipitation, Materials (Basel) 12 (2019), doi:10.3390/MA12244083.

[21] B. Milkereit, M. Beck, M. Reich, O. Kessler, C. Schick, Precipitation kinetics of an aluminium alloy during Newtonian cooling simulated in a differential scanning calorimeter, Thermochim. Acta. 522 (2011) 86–95, doi:10.1016/j.tca.2011.02.034.

[22] B. Milkereit, L. Jonas, C. Schick, O. Keßler, Das kontinuierliche Zeit-Temperatur-Ausscheidungs-Diagramm einer Aluminiumlegierung EN AW-6005A, J. Heat Treat. Mater. HTM = Zeitschrift Für Werkstoffe, Wärmebehandlung, Fert. 65 (2010) 171, doi:10.3139/105.110056.

[23] R.H. Kemsies, B. Milkereit, S. Wenner, R. Holmestad, O. Kessler, situ DSC investigation into the kinetics and microstructure of dispersoid formation in Al-Mn-Fe-Si(-Mg) alloys, Mater. Des. 146 (2018) 96–107, doi:10.1016/j.matdes.2018.03.007.

[24] D. Turnbull, Transient Nucleation, Trans. Am. Inst. Mining, Metall. Pet. Eng. 175 (1948) 774–783.

[25] E. Kozeschnik, Modelling Solid-State Precipitation, Momentum Press, LLC, New York, New York, 2013. https://doi.org/10.5643/9781606500644.

[26] B. Sonderegger, E. Kozeschnik, Generalized Nearest-Neighbor Broken-Bond Analysis of Randomly Oriented Coherent Interfaces in Multicomponent Fcc and Bcc Structures, Metall. Mater. Trans. A Phys. Metall. Mater. Sci. 40 (2009) 499–510, doi:10.1007/s11661-008-9752-6.

[27] B. Sonderegger, E. Kozeschnik, Size dependence of the interfacial energy in the generalized nearest-neighbor broken-bond approach, Scr. Mater. 60 (2009) 635–638, doi:10.1016/j.scriptamat.2008.12.025.

[28] B. Sonderegger, E. Kozeschnik, Interfacial energy of diffuse phase boundaries in the generalized broken-bond approach, Metall. Mater. Trans. A Phys. Metall. Mater. Sci. 41 (2010) 3262–3269, doi:10.1007/s11661-010-0370-8.

[29] N. Saunders, A.P. Miodownik, CALPHAD (calculation of phase diagrams): a comprehensive guide, Elsevier, 1998.

[30] N.H.H. van Dijk, S.E.E. Offerman, J. Sietsma, S. van der Zwaag, Barrier-free heterogeneous grain nucleation in polycrystalline materials: The austenite to ferrite phase transformation in steel, Acta Mater 55 (2007) 4489–4498, doi:10.1016/j.actamat.2007.04.013.

[31] H. Song, J.J. Hoyt, Barrier-Free Nucleation at Grain-Boundary Triple Junctions during Solid-State Phase Transformations, Phys. Rev. Lett. 117 (2016) 1–5, doi:10.1103/PhysRevLett.117.238001.

[32] D. Hull, D.J. Bacon, Introduction to dislocations., Elsevier. 37 (2011).

[33] P.J. Clemm, J.C. Fisher, The influence of grain boundaries on the nucleation of secondary phases, Acta Metall 3 (1955) 70–73, doi:10.1016/0001.6160(55)900146.

[34] W.C. Johnson, C.L. White, P.E. Marth, P.K. Ruf, S.M. Tuominen, K.D. Wade, K.C. Russell, H.I. Aaronson, Influence of crystallography on aspects of solid-solid nucleation theory, Metall. Trans. A. 6 (1975) 911–919, doi:10.1007/BF02672315.

[35] W.F. Lange, M. Enomoto, H.I. Aaronson, Precipitate nucleation kinetics at grain boundaries, Int. Mater. Rev. 34 (1989) 125–150, doi:10.1179/imr.1989.34.1.125.

[36] B. Milkereit, M.J. Starink, Quench sensitivity of Al-Mg-Si alloys: A model for linear cooling and strengthening, Mater. Des. 76 (2015) 117–129, doi:10.1016/j.matdes.2015.03.055.

[37] P. Schumacher, S. Pogatscher, M.J. Starink, C. Schick, V. Mohles, B. Milkereit, Quench-induced precipitates in Al-Si alloys: Calorimetric determination of solute content and characterisation of microstructure, Thermochim. Acta. 602 (2015) 63–73, doi:10.1016/j.tca.2014.12.023.

[38] L.E. Murr, Interfacial phenomena in metals and alloys, CBLS Publ., Marietta, Ohio, 1978. https://doi.org/10.1016/0390-6035(78)90059-7.

[39] Y. Huang, F.J. Humphreys, Measurements of grain boundary mobility during recrystallization of a single-phase aluminium alloy, Acta Mater 47 (1999) 2259–2268, doi:10.1016/S1359-6454(99)00062-2.

[40] M.A. Tschopp, D.L. McDowell, Asymmetric tilt grain boundary structure and energy in copper and aluminium, Philos. Mag. 87 (2007) 3871–3892, doi:10.1080/14786430701455321.

[41] B. Sonderegger, E. Kozeschnik, Interfacial Energy of Diffuse Phase Boundaries in the Generalized Broken-Bond Approach, Metall. Mater. Trans. A Phys. Metall. Mater. Sci. 41 (2010) 3262–3269, doi:10.1007/s11661-010-0370-8.

[42] W. Huang, M. Hillert, The role of grain corners in nucleation, Metall. Mater. Trans. A Phys. Metall. Mater. Sci. 27 (1996) 480–483, doi:10.1007/BF02648428.

[43] Y. Huang, F.J. Humphreys, The effect of solutes on grain boundary mobility during recrystallization and grain growth in some single-phase aluminium alloys, Mater. Chem. Phys. 132 (2012) 166–174, doi:10.1016/j.matchemphys.2011.11.018.

[44] E. Kozeschnik, Mean-Field Microstructure Kinetics Modeling, Encycl. Mater. Met. Allloys. 4 (2022) 521–526, doi:10.1016/b978-0-12-819726-4.00055-7.

[45] B. Milkereit, Kontinuierliche Zeit-Temperatur- Ausscheidungs-Diagramme von Al-Mg-Si-Legierungen, Universität Rostock, 2010.

[46] Y.J. Li, L. Arnberg, Quantitative study on the precipitation behavior of dispersoids in DC-cast AA3003 alloy during heating and homogenization, Acta Mater 51 (2003) 3415–3428, doi:10.1016/S1359-6454(03)00160-5.

[47] C. Li, K. Liu, N. Parson, X.-G. Chen, The effect of heat treatments on precipitation behavior of dispersoids in Al-Mg-Si-Mn ALLOY, Proc. 16th Int. Alum. Alloy. Conf. 2018. (2018).

[48] L. Lodgaard, N. Ryum, Precipitation of dispersoids containing Mn and/or Cr in Al-Mg-Si alloys, Mater. Sci. Eng. A. 283 (2000) 144–152, doi:10.1016/s0921-5093(00)00734-6.